ADVANCES IN 3D IMAGE PROCESSING TO EVALUATE DAMAGE AND FRACTURE OF HIGH-PERFORMANCE CONCRETE

AIDAN R. CARLSON AND ERIC N. LANDIS

University of Maine
Orono, Maine, USA
e-mail: landis@maine.edu

Key words: X-ray CT, Fiber Reinforced Concrete, Rate Effects

Abstract. The three-dimensional images made possible by techniques such as x-ray computed tomography continue to provide us with new insights into fracture processes in concrete. Over the past 30 years, advances in both image acquisition and image analysis have improved to the point in which CT-based experiments are becoming relatively commonplace. In this work, we review some image analysis advancements and how they can be used to quantify the internal mechanisms that contribute to the complex problem of energy dissipation. The case study presented features a high-performance concrete with hybrid reinforcing consisting of conventional steel fibers, micro (steel wool) fibers, and a hybrid combination of both. 50-mm diameter specimens were loaded in a split-cylinder configuration at quasi-static and low-velocity impact rates. The 3D image analysis broke the crack measurement problem into two parts: macro-cracking and micro-cracking. In this case, macro-cracks were defined as those visible in the images, while micro-cracks were those not visible. An edge detection algorithm was employed to measure macro-cracks, while a digital volume correlation method was used to estimate micro-cracking. Results showed a shift in micro-crack to macro-crack ratio as strain rates increased, although the result are highly dependent on the nature and orientation of the fiber reinforcements.

1 INTRODUCTION

The tools for important measurements in concrete fracture are continuing to evolve rapidly. With respect to x-ray computed tomography (CT), advances have come both in the form of improved laboratory instruments that produce high spatial resolution, but also in computing hardware and software capacity that can handle larger and larger data sets. Only 25 years ago, a modest 500 by 500 by 500 voxel image would produce a data set of at least 125 MB, which would have overwhelmed a typical desktop PC hard drive. Now it is not uncommon for a single CT scan to produce a data set that exceeds 50 GB, which while still very large, can be handled readily with a high end desktop or even laptop computer. Similarly, the combination of hardware improvements and algorithmic advances allow us to complete 3D image analysis tasks in minutes to hours rather than days.

In this paper we review some of the key advances in three-dimensional image analysis that allow us to quantify the characteristics of damage and fracture in concrete. These advances are applied to the problem of rate-dependent fracture of a steel fiber reinforced high performance concrete subjected to split cylinder loading.

2 BACKGROUND

X-ray computed tomography (CT) has been applied to concrete and reinforced concrete for

over four decades. Early work focused on qualitative assessment of internal features [1,2], and basic trials of what where the capabilities of the technique. Recognition that analysis of the resulting 3D digital images could open up quantitative measurements of internal features led to applications of CT to fracture [3, 4], as well as porosity and pore structure [5]. In the case of fracture, when combined with *in situ* scanning, measurements of crack geometry were not limited only to surfaces. The afore mentioned quantitative analysis is realized through some basic image analysis steps, which are reviewed below. Additional techniques are detailed in section 3.

2.1 Review of basic 3D image analysis

Quantitative analysis is made possible through recognition that a 3D image is just an array of voxel intensities that are proportional to the x-ray absorption at that point. As x-ray absorption depends on elemental makeup, the voxel intensity can be linked to the material phase. This relationship is the basis for threshold-based segmentation, in which the image is separated by phase based on voxel intensity. For example, all voxels above a certain threshold are considered to be a solid phase, and all voxels below the threshold are considered to be an air or void (or crack) phase. A quantity such as porosity can be established by adding up all the "air" voxels inside the specimen and dividing that total by the total volume (air+solid) of the specimen. The challenge with this type of analysis is that choice of threshold between phases directly affects resulting measurement. Generally, a sensitivity analysis should be done on the measurements.

The next basic step useful for crack analysis (among other things) is a connectivity analysis. Connected component routines assess all the voxels of a particular phase, checking for whether they are in contact with other voxels of the same phase. Such adjacent voxels are considered part of the same object, such as a pore or a crack. Once the objects are identified, they can be quantified by volume (number of vox-

els) and surface area (number of voxel faces that form the boarder of the object. The volume is useful for something like pore size distribution, while the surface area is a key measurement in fracture energy. Such measurements can provide numerous insights into crack evolution as a damage-inducing load is applied [6]. It should be noted that measurement of cracking assumes there is a 'before' and 'after' image by which changes such as crack growth can be compared.

3 MEASUREMENTS OF CRACKING

The above mentioned image analysis steps were developed for the cited work on fracture that employed synchrotron radiation for the x-ray source. Such a source is provides extremely bright x-rays that leads to very high contrast images. Measurements of crack area could be done using a simple difference in surface area of all solid objects before and after a damage-inducing load was applied. This approach recognized that all changes in surface area were the result of fracture. It was found that while surface area measurement is sensitive to choice of threshold, the change in surface are was not so sensitive. Hence, the measurement was reasonably robust. Unfortunately conventional x-ray sources, which provide a majority of laboratory CT measurements, do not provide the level of contrast that a synchrotron does, so alternative measurements approaches must be applied. Below we focus on two levels of crack measurement: macro-cracking and micro-cracking. Macro-cracking is defined here as cracks that are visible in the CT image, while micro-cracking is defined as cracks that are below the resolution of the image and are therefore not visible.

3.1 Macro-crack measurements

A problem with a threshold-based approach to crack identification is that crack objects tend to be thin, and are susceptible to something called partial volume effect, where an individual voxel has more than one phase (e.g. solid and air). In such cases, the voxel will have an intensity somewhere between the two phases

making it overly sensitive to threshold value. In these cases it is better to look at the local gradient of voxel intensities to identify such objects. The Canny method is an effective method in which the image is first smoothed with a Gaussian filter, then the gradients are calculated, and finally the gradients are thresholded to establish edges. The crack surface area is taken as the difference in the total area of edges between the scans of an undamaged specimen and a damaged specimen. The process is illustrated in Fig. 1.
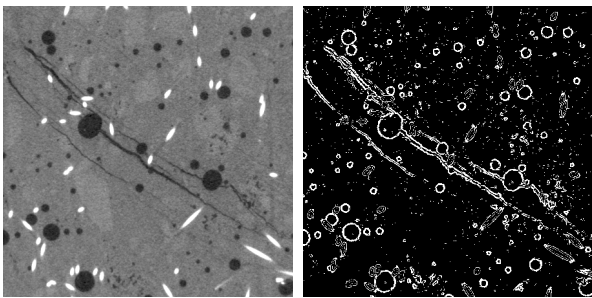

Figure 1: Illustration of edge detection with original slice (left) and processed slice (right). Note that the very strong edges from fibers have been removed via an upper threshold.

While not always a significant fracture measure, in this work we were interested in crack volumes. To do this we employed a simple thresholding and connected components procedure, followed by some filtering of the isolated objects. The process is illustrated in Fig. 2, where 2(a) shows a slice image, and 2(b) shows the segmented void and crack spaces. Note that an intermediate step is not shown, where the air (dark) outside the specimen boundary is omitted from the analysis. In order to focus on cracks alone, each isolated object (crack or pore) was analyzed for volume and surface area. Since cracks tend to have a high surface area-to-volume ratio, and air voids are the opposite, it is fairly easy to separate the two. The exception, however, is when a crack passes through or otherwise contacts an air void, as shown in Fig. 2(c). In order to exclude the air voids from crack analysis, we create a mask from the undamaged specimen that has the air voids with-

out the cracks. In the two images, any set of voxels that is the same in both images (i.e. when a crack object intersects a void object), the void object is removed from the crack object. The resulting crack measurement is shown in Fig. 2(d).
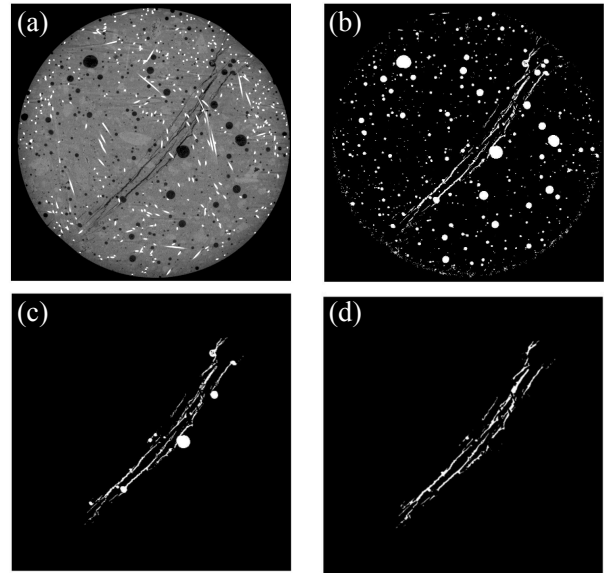

Figure 2: Illustration of macro-crack islolation.

3.2 Micro-crack analysis

As noted above, micro-cracks here are defined as those that are below the resolution of the CT instrument. Clearly a quantitative analysis of such cracks is limited. However, we find we can detect their effect due to the fact that when cracks close during unloading, they are unlikely to close completely. Thus, there is a residual strain that can be detected using digital volume correlation (DVC), and we can uses this measured residual strain as a proxy for degree of micro-cracking. DVC is an analysis technique that can produce a displacement map using a reference and a deformed volume image. It may be considered an extension of the well known 2D digital image correlation (DIC) technique. However, while DIC typically depends on the application of a random speckle pattern on a specimen surface, DVC relies on sufficient variation of the specimens internal structure to provide the contrast necessary to detect motion.

The output of DVC analysis is a vector displacement field, from which deformation or strain fields can be determined.

Given a reference image $F(X)$ and a deformed image $G(X)$, where X is a point in the volume, DVC seeks to determine a displacement image, $U(X)$ for which:

$$G(X + U(X)) = F(x) \tag{1}$$

The solution for $U(X)$ is generally arrived at through a least error optimization. However, the solution can still be challenging. Noise in the images can affect the result, and there are inevitably portions of an image (e.g. an air bubble), where there is insufficient contrast to identify any motion. A detailed solution procedure is beyond the scope of this paper, but an excellent summary can be found in the paper by Buljac *et al.* [7].

The analysis presented here consisted of several steps. First, the initial and the damaged images are registered with respect to each other. This puts them in a close initial alignment, which reduces the DVC computation time. The registration is also a correlation-based method, but the approach uses rigid body motion to align the images.
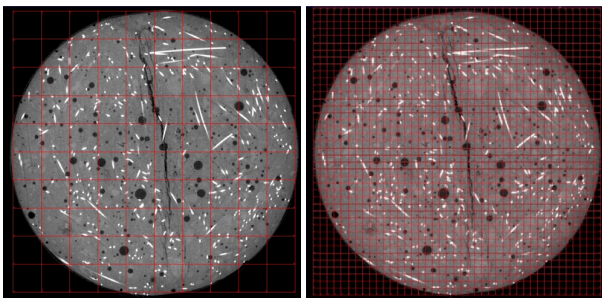

Figure 3: Illustration of coarse and fine grids for DVC analysis.

The next step is to subdivide the image into a series of sub-images, as illustrated in Fig. 3. The size of the sub-images is a trade-off, as a course grid provides high accuracy of motion, but at low resolution. As the size of the sub-images gets smaller, the resolution of the variations in displacements increases, but the likelihood of there being enough consistent contrast within the volume goes down. For this work, sub-images of 30 voxels on a side provided a reasonable trade-off.

An example of a DVC-based 3D vector field is shown in Fig. 4. From the resulting displacement fields, strain values were evaluated using a central difference approach. An example strain field is presented in Fig. 5. The image warrants several comments. First, it should be emphasized that while the image shown is 2D and shows ε_x, the full strain field is 3D. Second, it should be clear that around the crack the strain is smeared and the effect of the crack opening is simply a large strain. While we acknowledge this is not kinematically correct, as detailed below, it provided a useful way to account for impact of micro-cracking.
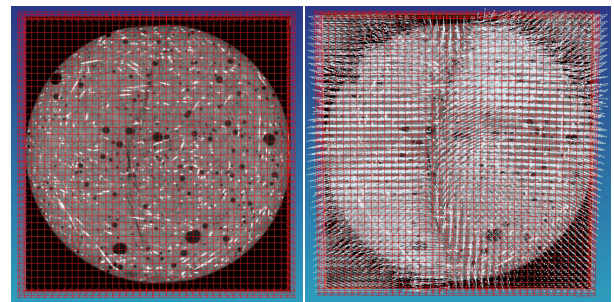

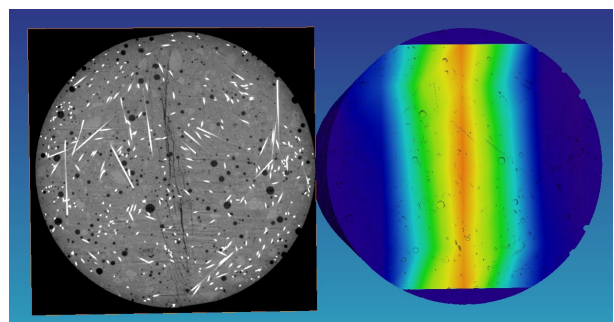Figure 4: Illustration fine mesh and corresponding displacement vectors.

Figure 5: Resulting strain field, ε_x for given slice image.

4   APPLICATION TO HPC FRACTURE

The analysis methods presented above were applied to a study of fracture of fiber-reinforced high-performance concrete subjected to split cylinder loading at different loading rates.

4.1 Concrete specimens

High performance concrete with a 115-120 MPa compressive strength was the material of interest in this study. More details of the material can be found in Rezakhani *et al.* [8]. All specimens had a mix proportion of 1: 0.31: 0.60: 1.72: 0.21, by weight cement: silica fume: slag: sand: water. Three different specimen types were cast in 50 mm by 100 mm cylinders: plain concrete, concrete reinforced with "macro" fibers (Bekaert OL 0.2-mm diameter/13-mm long brass-coated), concrete reinforced with "micro" fibers (steel wool with diameter varying from 10 and 200 μm and length varying from 0.3 to 4.8 mm), and concrete reinforced with a combination of micro and macro fibers. Details of fiber contents are provided in Table 1.

Table 1: Concrete and Fiber Types

Designation	Fiber Type	V_f (%)
OL	macro	2.0
SWOL	macro/micro	2.0/1.5

Specimens preparation consisted of mixing the cement matrix in a planetary mixer for five minutes, after which the fibers were added and mixed for an additional three minutes. Cast specimens were demolded after 24 hours, whereupon they were steam-cured at 90° for 72 hours. After cooling, the specimens were stored in ambient conditions until testing, which took place anywhere between 60 and 120 days. Each 50 by 100 mm cylinder was cut in half to form a set of two matched 50 by 50 mm nominal specimens. Each matched specimen pair was reassembled into its initial configuration prior to tomographic scanning.

4.2 X-Ray Computed Tomography

Prior to any mechanical testing, specimens were scanned with a laboratory-based x-ray CT scanner at 220 keV with a current of 245 μA. Tomographic scans consisted of 3770 projection images each being 2423 × 3770 pixels. Scanning time was 75 minutes. Tomographic reconstruction led to a series of 1200 × 1200 cropped slices at about 40 μm per voxel. An example slice images are shown in Fig. 6.
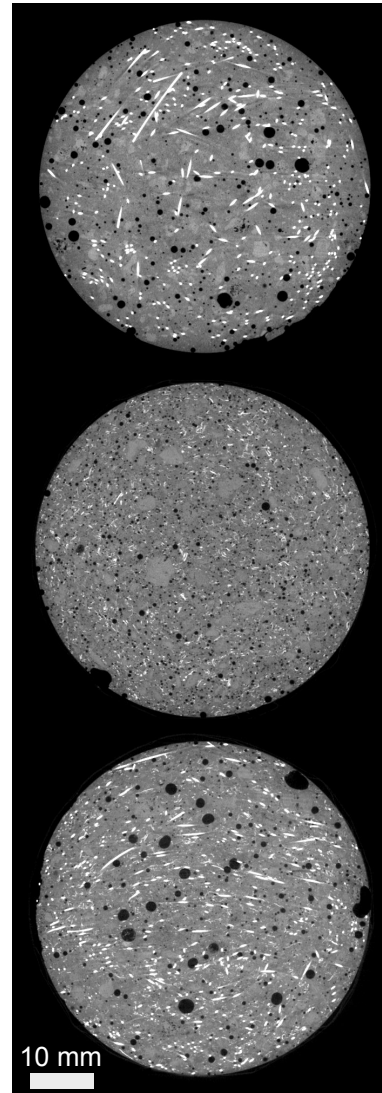

Figure 6: Example tomographic scans of concrete mixes. Top: steel fibers only, middle: steel wool only, bottom: steel fibers and steel wool

From the resulting 3D tomographic images, a macro fiber orientation analysis was done for each specimen. The issue is that even a seemingly random fiber orientation is likely to have preferential alignments that can be significant [9, 10]. In this analysis, the spatial orientation of each fiber is evaluated and compared to possible load axes in a split cylinder configuration. An optimum orientation is defined as the position the fibers provide the most efficient rein-

forcement relative to the principal tensile stress. Conversely, a pessimum orientation is defined as that in which the fibers provide the least efficient reinforcement [11]. The intent of the optimum/pessimum analysis is to provide bounds on any subsequent analysis as to the role of fiber orientation on the result.

4.3 Mechanical Testing

After initial tomographic scan and fiber orientation assessment, each specimen was subjected to split cylinder loading. Two different loading rates were used:

- quasi-static ($\dot{\varepsilon} \approx 1 \times 10^{-3}$/s)
- intermediate ($\dot{\varepsilon} \approx 1 \times 10$/s)

Both cases were carried out on a servo-hydraulic load frame, while the third being performed on a drop weight tower. For the servo-hydraulic tests, position control was used. Load was recorded with a dynamic-calibrated load cell, and platen-to-platen displacement was recorded using a pair of LVDTs.

4.4 Data Analysis

Analysis of mechanical testing data is fairly straightforward, with the primary parameter of interest being energy dissipated by the specimen. For the servo-hydraulic-loaded specimens, this is simply established by taking the area under the load-deformation curve and subtracting the area of elastic recovery.

Image analysis was conducted using the techniques detailed in section 3. The basic steps here were edge detection and digital volume correlation using before and after loading images, and crack volume measurements using the damaged images. The focus of the analysis described here was the reconciliation of the DVC analysis and the crack volume analysis. Of particular interest was the contribution of the total volumetric strain, as measured using DVC, and the contribution of the measured macro-crack volume.

Volumetric strain was calculated from the DVC-measured strain fields. Specifically, if we

define volumetric strain, $\Delta V/V$ as:

$$\frac{\Delta V}{V} = \varepsilon_y + \varepsilon_y + \varepsilon_z \quad (2)$$

Given that the strain values are measured at discrete points for a particular subvolume, the change in specimen volume is then written as:

$$\frac{\Delta V}{V} = \frac{1}{V} \sum_{i=1}^{N} \left(\varepsilon_{xi} + \varepsilon_{yi} + \varepsilon_{zi} \right) V_i \quad (3)$$

where V_i is the volume of the ith subvolume, and N is the number of such subvolumes.

5 RESULTS

The measured energy dissipation is summarized in Table 2, where OL refers to fiber reinforced specimens, SWOL refers to combined steel wool and fiber reinforced specimens. In each case there is a result for static loading rate ('Low') and high loading rate ('high'). The results are further split by optimum and pessimum specimen orientations.

Table 2: Specimen Energy Dissipation, U

Specimen	U (J)
OL-High-Opt	39.8
OL-High-Pes	37.6
OL-Low-Opt	30.2
OL-Low-Pes	31.3
SWOL-High-Opt	49.6
SWOL-High-Pes	33.5
SWOL-Low-Opt	36.3
SWOL-Low-Pes	29.8

From these results we observe that with one exception, optimum-oriented specimens produced higher energy absorption than pessimum-oriented specimen. Also, with exceptions, the steel wool specimens dissipated more energy than the counterparts without steel wool.

The total volumetric strain, $\Delta V/V$, was calculated from DVC analysis and eq. 3, while the total volume of macro-cracking for each specimen was calculated from the connected component analysis. For comparison purposed, the macro-crack volume can be reported as an equivalent volumetric strain, $\Delta V_M/V$. This

equivalent strain is established by simply dividing the volume of the macro-cracks by the volume of the specimen. In this way, the contribution of macro-cracking can be separated from micro-cracking, with the volumetric strain due to micro-cracking simply being the total strain less the macro-cracking strain, or:

$$\frac{\Delta V_\mu}{V} = \frac{\Delta V}{V} - \frac{\Delta V_M}{V} \qquad (4)$$

where $\Delta V_\mu/V$ is the equivalent volumetric strain to to microcracking. The results of this analysis are presented in Table 3. In order to account for the differences in actual energy dissipated by the different specimens, each of these strain values have been normalized by the energy dissipation presented in Table 2.

Table 3: Specimen Volume Changes

Specimen	$\Delta V/V$	$\Delta V_M/V$	$\Delta V_\mu/V$
OL-High-Opt	0.0096	0.0074	0.0022
OL-High-Pes	0.0544	0.0117	0.043
OL-Low-Opt	0.0120	0.0052	0.0066
OL-Low-Pes	0.0072	0.0067	0.0005
SWOL-High-Opt	0.0102	0.0054	0.0048
SWOL-High-Pes	0.0089	0.0065	0.0024
SWOL-Low-Opt	0.0077	0.0057	0.0020
SWOL-Low-Pes	0.0074	0.0073	0.0001

The relative strain values are better visualized through the charts of Figs. 7 and 8, where the normalized total volumetric strain is broken down by macro-cracking and micro-cracking. Here, several distinct trends are highlighted. In the specimens with only fiber reinforcement, (Fig. 7) the trends are clear. Regardless of loading rate, optimally oriented specimens show lower overall volumetric change. What is more interesting, however, is that the increase in volumetric change in the pessimum-oriented specimens is entirely due to macro-crack opening. This is especially pronounced in the quasi-static specimen which shows almost now residual strain due to micro-cracking.

Nearly the entire volumetric change can be attributed to macro-crack opening. An additional observation, though less pronounced, is that the specimens loaded at a higher rate show a higher degree of micro-cracking relative to macro-cracking. This holds for both the optimum and the pessimum-oriented specimens.
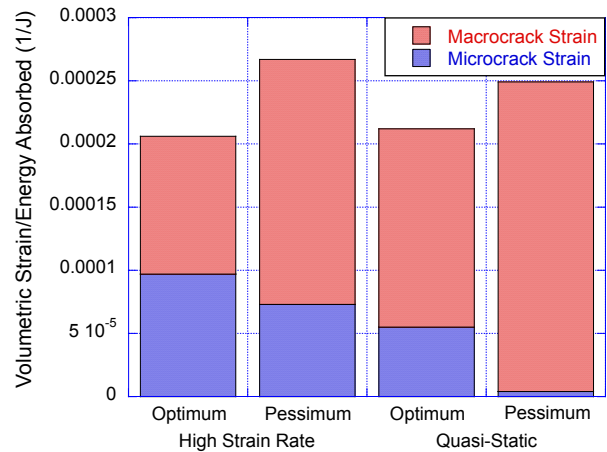

Figure 7: Relative distributions of micro-cracking versus macro-cracking at different loading rates for fiber reinforcement only.
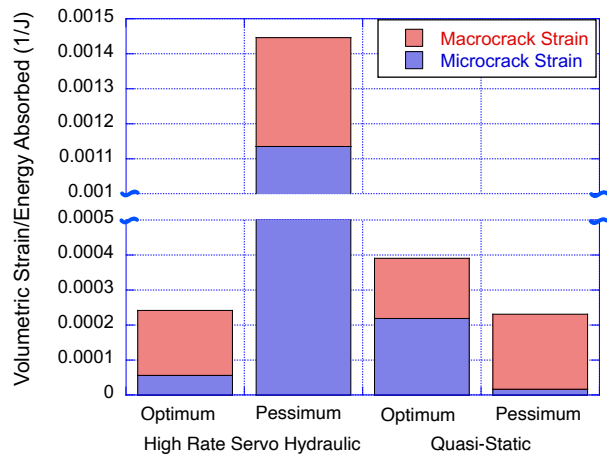

Figure 8: Relative distributions of micro-cracking versus macro-cracking at different loading rates for fiber reinforcement plus steel wool.

For the specimens with steel wool reinforcement, (Fig. 8), the trends are not so clear. First, there is an extreme outlier in the high-rate-loaded pessimen specimen, which showed more than three times more volumetric strain than any

other specimen, and a majority of this increase was in micro-cracking. Second, for the quasi-static tests, the volumetric strain was higher in the optimum than the pessimum, although the shift between micro-cracking and macro-crack distribution was consistent with the other specimens. We have no explanation for the high strain of the high rate pessimum-oriented specimen.

6 Discussion

While the primary goal of this work was to quantify differences in energy dissipation mechanisms as a function of loading rate, we find that while there are measurable differences, these differences are within the bounds of differences that arise simply from differences in fiber orientation distribution.

The observed differences in microcracking versus macrocracking are best illustrated in the 3D renderings of Fig. 9. Here, we qualitatively observe how in the optimum-oriented specimen (Fig. 9a) the main tensile crack is not as wide, and tends to meander more compared to the pessimum-oriented specimen (Fig. 9b). This suggests that in the optimum-oriented specimens, the more advantageous fiber alignment makes it more difficult to open the macrocrack, forcing energy dissipation towards the formation of more microcracks. The exact same observation is made in comparing the observed changes when the loading rate is increased. At high loading rate, a higher degree of microcracking is observed regardless of the specimen orientation.

The observed differences in microcrack/macrocrack formation suggest differences in energy dissipation mechanisms. Crack formation, regardless of scale, represents an energy conversion in which strain energy is dissipated by formation of new surfaces. In the case of advancing macrocracks, there is a shift from surface formation (crack propagation) to crack opening. For fiber-reinforced composites, kinematically, crack opening means that fibers are being stretched and pulled out of the cement matrix, inducing a separate energy dissipation

mechanism. Thus, we can conclude that both at low load rates and less-than-ideal fiber orientations, a much higher fraction of energy dissipation is provided by fiber pullout phenomena, such as debonding and friction. At high load rates and more ideal fiber orientations, however, we see a greater fraction of energy dissipation through matrix cracking.
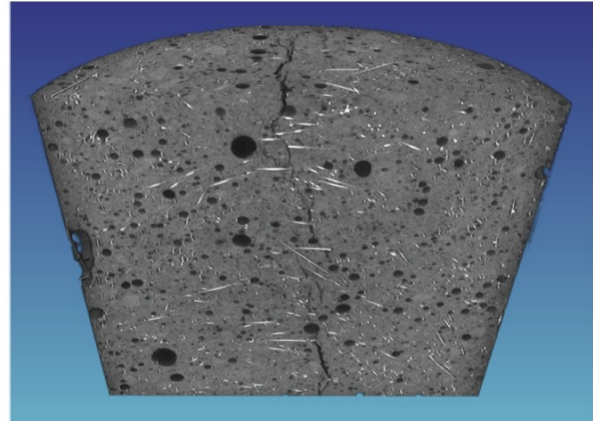
(a) Optimum-oriented specimen
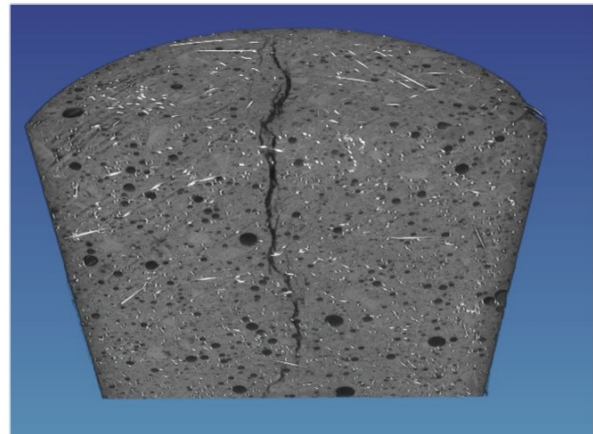
(b) Pessimum-oriented specimen

Figure 9: 3D renderings of internal cracking for: (a) optimum-oriented specimen and (b) pessimum-oriented specimen.

While the above observations are empirical, they do not necessarily address the root causes of the shift. From a load rate perspective, we can propose here that the shift in macrocrack-to-microcrack could have an inertial basis in that crack opening requires substantial rigid body motion, while microcracking does not. Hence, at higher rates the path of least resis-

tance is to create more microcracks, while at lower loading rates, when the inertial effects approach zero, the path of least resistance is to open up existing cracks.

With respect to the fiber orientation effect, it may be more simple. A poorly aligned set of fibers does not have the capacity to bridge macrocracks as well, so the crack can be opened more easily, negating the need to shift to additional microcracking. Indeed, in the results presented in Fig. 7, the fraction of microcracking is almost negligible, with macrocrack opening accounting for nearly all of the volumetric increase.

It must be noted that our microcrack/macrocrack definition is completely arbitrary, driven by the resolution of imaging capabilities. However, we suggest that it is likely that similar shifts would be observed at other scales, but we would likely see changes in the specific microcrack/macrocrack distributions.

7 CONCLUSIONS

In this work we employed x-ray CT imaging of undamaged and damaged fiber-reinforced high performance concrete specimens subject to split cylinder loading at different rates. The primary question to be answered was how the energy dissipation mechanisms during damage and fracture are affected by loading rate. Using a combination of 3D image processing techniques, two different damage types were designated: microcrack and macrocrack. 3D digital volume correlation was employed to measure the overall residual (inelastic) deformation of the specimens after testing. Concurrently, macrocracks, as defined as those cracks that were visible in the CT images, were isolated and measured, with a particular focus on the contribution of the macrocrack to the overall residual strain. A microcrack was then defined as anything that contributed to residual strain that was not measured as a macrocrack.

The results show distinct shift at higher loading rates, with a higher fraction of microcracking occurring at higher loading rates. This phenomenon was attributed to the inertial effects on macrocrack formation.

However, a distinct shift in microcrack/macrocrack distribution was also observed for matched specimens loaded at different orientations that maximize (optimum) or minimize (pessimum) the degree in which fibers are in a position to efficiently bridge cracking. At the optimum orientation, we see a higher contribution of microcracking compared to the pessimum orientation. This shift was attributed to the relative inefficiency of fiber bridging, easing macrocrack growth.

An important conclusion here is that while rate effects were seen in the damage patterns, the degree of variation between low and high rate loading was of a comparable magnitude as the degree of variation between optimum and pessimum specimen orientation. Thus, we cannot overemphasize the importance of taking fiber orientation into account in both modeling of such materials, or in the interpretation of experimental results.

REFERENCES

[1] Morgan, I.L., Ellinger, H., Klinksiek, R., & Thompson, J.N. 1980. Examination of concrete by computerized tomography. *ACI Journal* **77**(1): 23–27.

[2] Martz, H.E., Scheberk, D.J., Roberson, G.P., & Monteiro, P.J. 1993. Computerized tomography analysis of reinforced concrete. *ACI Materials Journal* **90**(3): 259–264.

[3] Landis, E.N., Nagy, E.N., Keane, D.T., & Nagy, G. 1999. Technique to measure 3d work-of-fracture of concrete in compression. *Journal of Engineering Mechanics* **125**(6): 599–605.

[4] Landis, E.N. & Nagy, E.N. 2000. Three-dimensional work of fracture for mortar in compression. *Engineering Fracture Mechanics* **65**(2-3): 223–234.

[5] Landis, E.N.. Petrell, A.L., Lu, S. & Nagy, E.N. 2000. Examination of pore structure

using three dimensional image analysis of microtomographic data. *Concrete Science and Engineering* **2**(8): 162–169.

[6] Landis, E.N., Zhang, T., Nagy, E.N., Nagy, G., & Franklin, W.R. 2007. Cracking, damage and fracture in four dimensions. *Materials and Structures* **40**: 357–364. DOI 10.1617/s11527-006-9145-5.

[7] Buljac, A., Jailin, C., Mendoza, A. et al. 2018. Digital Volume Correlation: Review of Progress and Challenges. *Experimental Mechanics* **58**: 661–708. DOI: 10.1007/s11340-018-0390-7.

[8] Rezakhani, R., Scott, D.A., Bousikhane, F., Pathirage, M., Moser, R.D., Green, B.H., and Cusatis, G. 2021. Influence of steel fiber size, shape, and strength on the quasi-static properties of ultra-high performance concrete: Experimental investigation and numerical modeling. *Construction and Building Materials* **296**: 04016101. DOI: 10.1016/j.conbuildmat.2021.123532.

[9] Oesch, T.S., Landis, E.N., Kuchma, D.A. 2016. Conventional Concrete and UHPC Performance–Damage Relationships Identified Using Computed Tomography. *Journal of Engineering Mechanics* **142**(12): 04016101. DOI: 10.1061/(ASCE)EM.1943-7889.0001168.

[10] Oesch, T.S., Landis, E.N., Kuchma, D.A. 2018. A methodology for quantifying the impact of casting procedure on anisotropy in fiber-reinforced concrete using X-ray CT. *Materials and Structures* **51**: 1–13. DOI: 10.1617/s11527-018-1198-8.

[11] Landis, E.N., Kravchuk, R., Loshkov, D. 2019. Experimental investigations of internal energy dissipation during fracture of fiber-reinforced ultra-high-performance concrete. *Frontiers of Structural and Civil Engineering* **13**: 190–200. DOI: 10.1007/s11709-018-0487-1.